

# RaLL: End-to-end Radar Localization on Lidar Map Using Differentiable Measurement Model

Huan Yin, *Member, IEEE*, Yue Wang, *Member, IEEE*, Runjian Chen, and Rong Xiong, *Member, IEEE*

**Abstract**—Radar sensor provides lighting and weather invariant sensing, which is naturally suitable for long-term localization in outdoor scenes. On the other hand, the most popular available map currently is built by lidar. In this paper, we propose a deep neural network for end-to-end learning of radar localization on lidar map to bridge the gap. We first embed both sensor modals into a common feature space by a neural network. Then multiple offsets are added to the map modal for similarity evaluation against the current radar modal, yielding the regression of the current pose. Finally, we apply this differentiable measurement model to a Kalman filter to learn the whole sequential localization process in an end-to-end manner. To validate the feasibility and effectiveness, we employ multi-session multi-scene datasets collected from the real world, and the results demonstrate that our proposed system achieves superior performance over 90km driving, even in generalization scenarios where the model training is in UK, while testing in South Korea. We also release the source code publicly<sup>1</sup>.

**Index Terms**—Radar Localization, Deep Learning, Differentiable Model, Kalman Filter

## I. INTRODUCTION

LOCALIZATION is a fundamental component in autonomous robot system. A basic technique is to localize the robot via GPS/INS in outdoor scenes, which is infeasible in GPS-denied environments. Localization can also be accumulated by odometry data, while it is impracticable when the drift error becomes significant. Therefore, localization on pre-built map is indispensable, which tracks the robot pose with bounded uncertainty.

Recently many visual and lidar based approaches have been widely proposed in the field of robotics, but there still exist some difficulties in real applications. For instance, visual localization on visual map [1], [2] and lidar map [3] are still challenging when appearance changes significantly, like weather or season varies. For lidar localization, the technique

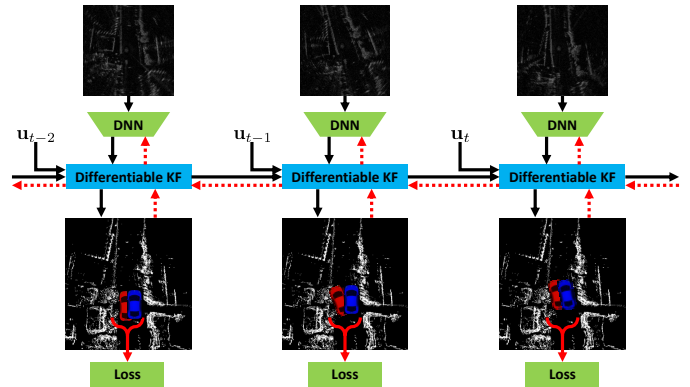


Fig. 1. The schematics of RaLL. The blue vehicle stands for the estimated pose from RaLL, and the red for the ground truth pose. The dash line indicates the back-propagation of gradient from sequential loss to learnable deep network.

is more mature, pose estimation can be achieved across day and night via point cloud registration [4]. Therefore, city scale lidar maps have been built for preparing of commercial application [5], [6]. Unfortunately, in extreme weather conditions [7], like foggy and snowy, the lidar range measurements are very noisy, calling for the aid of other sensors.

To build a robust localization system, we consider radar is a good choice, which is naturally lighting and weather invariant. Therefore, radar odometry becomes a research focus recently [8]–[12], and radar simultaneous localization and mapping [13]. A general idea is to build a map using radar, then localize the robot by aligning the radar measurements against the radar map. Considering that the large scale lidar map is available, we argue that repeating the whole mapping process for radar is extremely time and manual labor consuming, also bringing extra calibration between radar map and lidar map [14].

In this paper, we propose an end-to-end learning system to achieve **R**adar **L**ocalization directly on **L**idar map (RaLL), as shown in Figure 1. There are two challenges for RaLL. First, the common feature space of the two sensor modals is not explicitly supervised. We propose a network to learn the feature shared embeddings from the pose supervision by introducing a differentiable pose estimator to back-propagate the gradient. Second, the measurement uncertainty is not explicitly supervised, preventing the probabilistic fusion between measurement and motion. We apply the learned model above as a measurement model in a pose tracking Kalman filter (KF), enforcing the measurement uncertainty to be compatible to Gaussian fusion. By modeling the whole localization process

Manuscript received Month xx, 2xxx; revised Month xx, xxxx; accepted Month x, xxxx.

This work was supported in part by the National Key R&D Program of China (2019YFB1309500), and in part by the National Nature Science Foundation of China (61903332).

Huan Yin, Yue Wang, Runjian Chen and Rong Xiong are with the State Key Laboratory of Industrial Control and Technology, Zhejiang University, Hangzhou, China, and with the Institute of Cyber-Systems and Control, Zhejiang University, Hangzhou, China. (Corresponding author: Yue Wang)

<sup>1</sup>The code of RaLL is available at <https://github.com/ZJUYH/RaLL> and a video demonstration is available at <https://youtu.be/a3wEv-eVlcg>.

as a sequential Gaussian distribution estimator, we can supervise the measurement uncertainty via maximizing likelihood. To evaluate the system performance, we utilize RobotCar dataset [15], [16] for benchmark. Besides, the MulRan dataset [17] is employed for testing the generalization of RaLL. In summary, the contributions of this paper are as follows:

- A deep neural network architecture is proposed to learn the cross-modal shared feature embedding by back-propagating gradient from the pose supervision, which leverages the lidar map for radar localization.
- With the learned network being a differentiable measurement model, a Kalman filter is proposed to generate fused estimation, which is learned in an end-to-end way for improve the accuracy.
- We conduct the model training and testing using RobotCar driving dataset (UK), and achieve similar experimental performance in Mulran dataset (South Korea), demonstrating good generalization of RaLL.

The rest of this paper is organized as follows: Section II reviews the related topics in recent years. The whole system is introduced in Section III. Section IV reports the experimental results on two datasets. We conclude a brief overview on our system and a future outlook in Section V.

## II. RELATED WORK

**Localization using radar sensor.** Radar sensor has been applied for various perception tasks widely in autonomous driving area, mainly focused on dynamic objects detection on roads. Some researchers achieved indoor positioning using low-cost radar sensor, including localization on CAD model [18] or laser map [19]. But in challenging outdoor scenarios, precise radar localization is blocked by diverse types of sensor noises and Doppler velocity, therefore, most of studies are based on data pre-processing and sensor modeling [20]–[23].

Recently the Navtech Frequency Modulated Continuous Wave (FMCW) radar sensor brings less Doppler effect, higher resolution and 360°-view in data collection [13], [15]–[17]. The development of this sensor technique results in new approaches to robot localization research. For place recognition, part of positioning system, researchers extended the existing methods in vision or lidar community to radar data [17], [24]. As for ego-motion estimation, sparse landmarks and keypoints are extracted manually to build efficient data association model [8], [9], and these salient keypoints or pixels can also be learned by neural networks in [10], [25]. The state-of-the-art odometric performance was presented in [11], in which an end-to-end radar odometry system was proposed with the supervision of ground truth poses.

Considering the unavoidable drift in odometry, the registration between live scan and prior map is still essential for long-term localization. Hong et al. [13] used conventional SLAM algorithms to build a radar mapping system. Localization with multiple sensor modalities was presented in [26], in which radar data is localized against satellite image with a coarse initial estimate. The authors then presented more accurate results using multiple networks in [27]. In [28], to connect radar scan and lidar map, a generative adversarial network

(GAN) was used to transfer the radar to fake lidar data, and then Monte Carlo localization was applied for pose tracking.

**Deep learning for localization.** With the advances of deep learning, some geometric or theoretical problems of robot localization were solved by data-driven [29], [30]. A direct way is to localize the sensor by end-to-end learning without geometric information [31], which requires large training data to avoid overfitting. Some researchers [32] established feature correspondences by deep learning and used traditional solvers for pose estimation, while these solvers are indifferentiable for end-to-end learning.

This paper is inspired by several recent deep learning based approaches [5], [6], [11]. In these research works, localization is performed on same sensor modalities. While in this paper, we model the similarity measure and pose regression on the different modalities via deep neural networks. We also train and test the networks with the sequential data, thus building an end-to-end localization system in time domain.

## III. METHODS

The framework of RaLL is a differentiable Kalman filter embedded with a neural network based measurement model, which is introduced in Section III-C. The network architecture of the measurement model consists of two stages. The first stage embeds the radar scan and lidar map into a common feature space, which is introduced in Section III-A. The second stage evaluates the similarity of the features extracted from two branches above, and yield the final estimation, which is introduced in Section III-B. Finally, we show the training strategy for RaLL in Section III-D.

### A. Comparable Feature Embeddings

We represent both radar scan and lidar map as bird-eye view images. At time  $t$ , one scan  $\mathbf{R}_t^{H \times W}$  is generated from the radar, and an initial estimation of the pose is  $\mathbf{x}_t \in SE(2)$ . For the prior 2D laser map  $\mathbf{M}$ , we crop it to  $\mathbf{M}_t^{H \times W}$  at pose  $\mathbf{x}_t$ . With the input  $\mathbf{R}_t$  and  $\mathbf{M}_t$ , a neural network  $\mathcal{F}$  is designed to estimate the offset  $\Delta \mathbf{x} = \{\Delta x, \Delta y, \Delta \theta\}$  between  $\mathbf{x}_t$  and the ground truth pose  $\mathbf{x}_t^*$ . Therefore, the ground truth offset  $\Delta \mathbf{x}^*$  is the supervision for training  $\mathcal{F}$ .

There are three differences between the data from radar and lidar map, which prevents the direct alignment. First, various types of noises exist in radar data, while the lidar map is much cleaner. Second, there are occlusions in current the current scan, while the lidar map is more completed because of the multi-frame integration. Finally, the raw data forms are different:  $\mathbf{R}_t \in [0, 1]$  has continuous radar intensities while  $\mathbf{M}_t$  are represented by binary, or lidar grids. We embed the two heterogeneous modalities into a comparable feature space by training a deep neural network.

We establish a two-stream neural network for radar and lidar, shown in Figure 2. The whole network consists of three U-Net architectures [33], denoted as  $\mathcal{F}_m$ ,  $\mathcal{F}_r$  and  $\mathcal{F}_l$ . To suppress the noise in radar, we apply a masking network  $\mathcal{F}_m$  to learn a noise mask as in [11]. The sigmoid activation in the final layer constrains the masking output range to  $[0, 1]$ , then a de-noised representation  $\mathbf{R}_t^m$  is obtained by element-wise

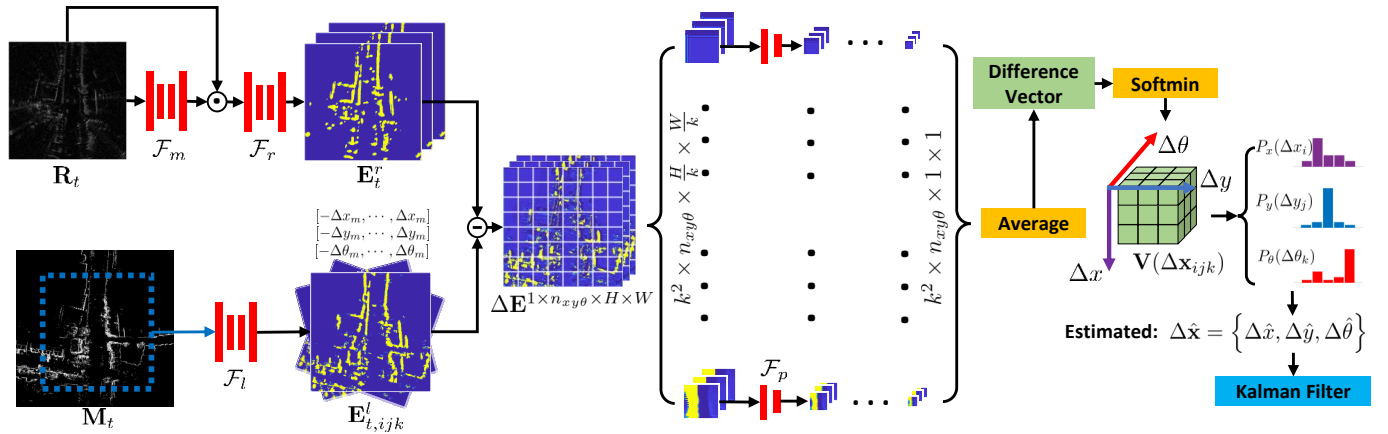


Fig. 2. The proposed network architecture of RaLL in this paper. This neural network  $\mathcal{F}$  consists of three U-Net  $\mathcal{F}_m, \mathcal{F}_l, \mathcal{F}_r$  and one patch network  $\mathcal{F}_p$ . Finally, the probability distributions of offsets are obtained, which are the measurements of the following KF system for pose tracking.

multiplication  $\mathbf{R}_t^m = \mathbf{R}_t \odot \mathcal{F}_m(\mathbf{R}_t)$ . We notice that the filtered  $\mathbf{R}_t^m$  is much clearer as shown in Fig. 3. Then we learn the feature embedding which is comparable between the de-noised radar scan and the lidar map:  $\mathcal{F}_r(\mathbf{R}_t^m) \mapsto \mathbf{E}_t^r, \mathcal{F}_l(\mathbf{M}_t) \mapsto \mathbf{E}_t^l$ . We set the final activation function as ReLU in  $\mathcal{F}_r$  and  $\mathcal{F}_l$  for feature extraction. Figure. 3 demonstrates several learned deep embeddings. It is clear that the features salient in both modalities, are directly comparable in the feature embedding space, such as buildings facade etc.

### B. Similarity based Offset Estimation

Given the initial pose  $\mathbf{x}_t$ , the pose offset should lie in a limited interval, denoted as  $-\Delta x_m \leq \Delta x \leq \Delta x_m, \Delta x_m > 0$ , the same for  $\Delta y$  and  $\Delta \theta$  in the range  $[-\Delta y_m, \Delta y_m]$  and  $[-\Delta \theta_m, \Delta \theta_m]$ . Then we divide the 3D solution space for the offset into grids with certain resolutions  $\delta x, \delta y, \delta \theta$ , and there are  $n_{xy\theta} = n_x \times n_y \times n_\theta$  candidates in total, e.g.  $n_x = \frac{\Delta x_m - (-\Delta x_m)}{\delta x} + 1$ . Hence each candidate in the solution space is denoted as  $\Delta \mathbf{x}_{ijk} = \{\Delta x_i, \Delta y_j, \Delta \theta_k\}$ , where  $1 \leq i \leq n_x, 1 \leq j \leq n_y, 1 \leq k \leq n_\theta$ . As a result, the absolute pose of each candidate is calculated by transform the initial pose  $\mathbf{x}_t$  using the offset  $\Delta \mathbf{x}_{ijk}$  as follow:

$$\mathbf{x}_t \boxplus \Delta \mathbf{x}_{ijk} = \begin{bmatrix} x_t + \cos(\theta_t + \Delta \theta_k) \Delta x_i - \sin(\theta_t + \Delta \theta_k) \Delta y_j \\ y_t + \sin(\theta_t + \Delta \theta_k) \Delta x_i + \cos(\theta_t + \Delta \theta_k) \Delta y_j \\ \theta_t + \Delta \theta_k \end{bmatrix} \quad (1)$$

At the level of feature embeddings, we rotate and translate the map embedding  $\mathbf{E}_t^l$  using  $n_{xy\theta}$  candidates, resulting in  $n_{xy\theta}$  map blocks  $\mathbf{E}_{t,ijk}^l$ . When feature embedding is learned, the feature should be comparable by the subtraction ( $\mathbf{E}_t^r - \mathbf{E}_{t,ijk}^l$ ). Repeating the subtraction for each candidate, we form a difference tensor as  $\Delta \mathbf{E}$  with the size  $n_{xy\theta} \times H \times W$

Considering the occlusion, we further divide  $\Delta \mathbf{E}$  into  $k \times k$  small patches as shown in Figure 2. For each patch, we utilize a patch network  $\mathcal{F}_p$  to derive a patch based difference. Finally, we average the  $k^2$  patch based differences and obtain a difference score between the radar scan feature  $\mathbf{E}_t^r$  and each candidate  $\mathbf{E}_{t,ijk}^l$ , leading to a difference vector with a length of  $n_{xy\theta}$ .

Essentially, if a candidate pose, say  $(\mathbf{x}_t \boxplus \Delta \mathbf{x}_{ijk})$  is close to the ground truth pose  $\mathbf{x}_t^*$ ,  $\mathbf{E}_t^r$  should be similar with  $\mathbf{E}_{t,ijk}^l$ , hence leading to a low difference at the  $ijk$ th position of the difference vector. As the lower the difference is, the closer the candidate and the ground truth lie, we take a softmin module to transform and normalize the difference vector to form a probability distribution. Then, we reshape the distribution into a 3-dimensional cost volume  $\mathbf{V}(\Delta \mathbf{x}_{ijk})$ . In summary, from the current radar scan and the lidar map, the proposed network produces a probability distribution of the pose offset to be estimated, states as follow:

$$\mathcal{F}_{m,r,l,p}(\mathbf{R}_t, \mathbf{M}, \mathbf{x}_t, \Delta \mathbf{x}_{ijk}) \mapsto \mathbf{V}(\Delta \mathbf{x}_{ijk}) \quad (2)$$

We then sum over the values along each axis to derive the marginal distribution:

$$\begin{cases} P_x(\Delta x_i) = \sum_{\Delta y_j, \Delta \theta_k} \mathbf{V}(\Delta \mathbf{x}_{ijk}) \\ P_y(\Delta y_j) = \sum_{\Delta x_i, \Delta \theta_k} \mathbf{V}(\Delta \mathbf{x}_{ijk}) \\ P_\theta(\Delta \theta_k) = \sum_{\Delta x_i, \Delta y_j} \mathbf{V}(\Delta \mathbf{x}_{ijk}) \end{cases} \quad (3)$$

Upon the marginal distribution, we design two losses to train the network:  $\mathcal{L}_1 + \mathcal{L}_2$ . When the estimation problem is regarded as three separated classification problems of  $\{\Delta x_i, \Delta y_j, \Delta \theta_k\}$ , a cross entropy loss can be formed as follows:

$$\mathcal{L}_1 = - \sum_{\Delta x_i} C_x \log(P_x) - \sum_{\Delta y_j} C_y \log(P_y) - \sum_{\Delta \theta_k} C_\theta \log(P_\theta) \quad (4)$$

where  $C_x, C_y$  and  $C_\theta$  are one hot encodings of the ground truth, which is the supervision. On the other hand, as a regression problem, we utilize the marginal expectations of the three marginal distributions as the estimators:

$$\Delta \hat{x} = \sum_{\Delta x_i} P_x \cdot \Delta x_i, \Delta \hat{y} = \sum_{\Delta y_j} P_y \cdot \Delta y_j, \Delta \hat{\theta} = \sum_{\Delta \theta_k} P_\theta \cdot \Delta \theta_k \quad (5)$$

and then the second loss is constructed by the squared error between the estimation  $\Delta \hat{\mathbf{x}}$  and ground truth  $\Delta \mathbf{x}^*$  as follows:

$$\mathcal{L}_2 = (\Delta \hat{x} - \Delta x^*)^2 + (\Delta \hat{y} - \Delta y^*)^2 + \alpha \cdot (\Delta \hat{\theta} - \Delta \theta^*)^2 \quad (6)$$

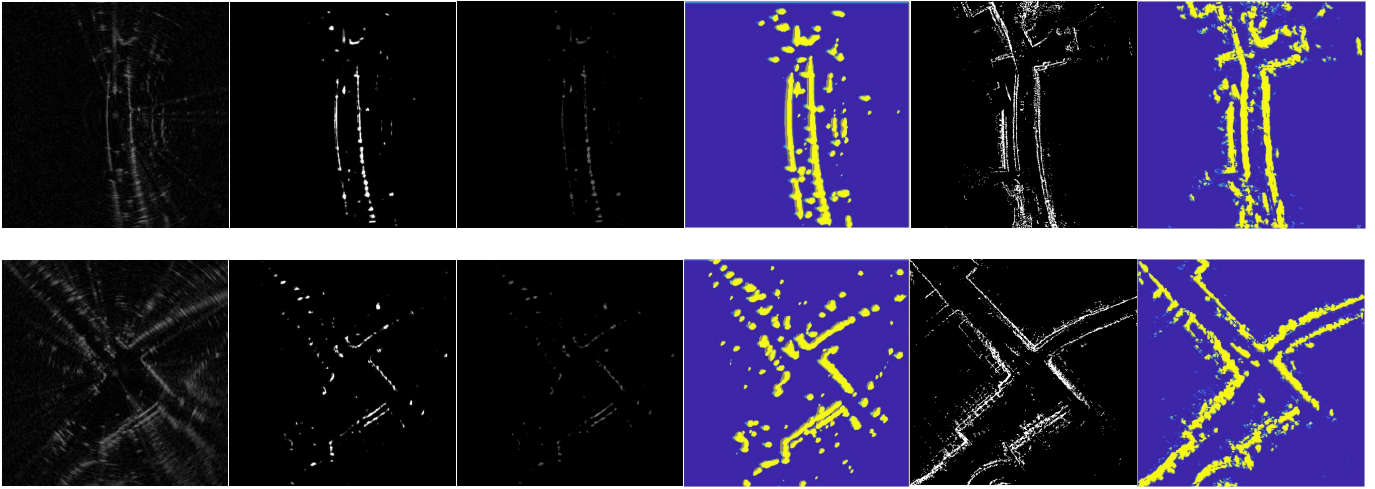


Fig. 3. From top to bottom: two scenes in RobotCar dataset. From left to right: the raw radar scan  $\mathbf{R}_t$ , the output from masking net  $\mathcal{F}_m(\mathbf{R}_t)$ , the multiplication results from masking  $\mathbf{R}_t^m$ , the deep embeddings of radar  $\mathbf{E}_t^r$ ; then followed the lidar map data  $\mathbf{M}_t$  and the deep embeddings  $\mathbf{E}_t^l$ . The radar and lidar data are generated at the same place for clearance.

where  $\alpha$  is a constant value to balance the translation metric ( $m$ ) and rotation angle metric ( $^\circ$ ).

### C. Differentiable Kalman Filter

Kalman filter is a general technique to fuse the sensor data in sequential. It consists of two steps, the prediction step using motion model and then followed by the updating step using measurement model, formulating a Bayesian recursive estimator with both models having Gaussian distributions.

Firstly, we propose an iterative closest point (ICP) based radar odometry as the motion model, which estimates the relative pose between two timestamps i.e.  $\mathbf{u}_{t-1}$  from  $\mathbf{R}_{t-1}$  to  $\mathbf{R}_t$ . Specifically, radar points with high intensities are extracted from the raw data, and an intensity threshold is used to select salient points. Then ICP [34] is performed on these filtered points to estimate the pose. Based on this radar odometry, the prediction step of is formulated as follows:

$$\begin{aligned} \bar{\mathbf{x}}_t &= f(\hat{\mathbf{x}}_{t-1}, \mathbf{u}_{t-1}) \\ \bar{\Sigma}_t &= \mathbf{F}_t \hat{\Sigma}_{t-1} \mathbf{F}_t^T + \Sigma_m \end{aligned} \quad (7)$$

where  $f(\cdot)$  accumulates the ego-motion on the previous estimated pose, and  $\mathbf{F}_t$  is the Jacobian of  $f(\cdot)$ . The covariance is also propagated and inserted with the odometry covariance  $\Sigma_m$ , which is a pre-defined coefficient.

In the update step, we utilize the networks  $\mathcal{F}_{m,r,l,p}$  as the measurement model. We estimate the offset  $\Delta \mathbf{x}_t$  at the predicted location  $\bar{\mathbf{x}}_t$ , then a global observation is generated by applying  $\mathbf{z}_t = \bar{\mathbf{x}}_t \boxplus \Delta \mathbf{x}_t$ . With this GPS-like observation, we can derive the measurement model. We also calculate the observation covariance  $\Sigma_o$  according to the probability distributions  $P_x, P_y$  and  $P_\theta$  derived above. Overall, the update step is formulated as follows:

$$\begin{aligned} \mathbf{K} &= \bar{\Sigma}_t (\bar{\Sigma}_t + \Sigma_o)^{-1} \\ \hat{\mathbf{x}}_t &= \bar{\mathbf{x}}_t + \mathbf{K}(\mathbf{z}_t - \bar{\mathbf{x}}_t) \\ \hat{\Sigma}_t &= (\mathbf{I} - \mathbf{K}) \bar{\Sigma}_t \end{aligned} \quad (8)$$

The network aided KF system is presented in Figure. 4. As both models are differentiable, the filter can be regarded as a recurrent network, which means that the measurement model can be trained by back-propagating gradients from future steps.

At the probabilistic perspective, KF generates the Gaussian posterior of the 3-dimensional pose in sequential, which is  $\mathcal{N}(\hat{\mathbf{x}}_t, \hat{\Sigma}_t)$ . Therefore, with the sequential ground truth pose  $\{\mathbf{x}_t^*\}$  available, we apply the maximum likelihood to tuning the network parameters as follows

$$\begin{aligned} &\text{maximize } \mathcal{N}(\mathbf{x}_t^*; \hat{\mathbf{x}}_t, \hat{\Sigma}_t) \\ &= \text{maximize } \frac{1}{\sqrt{(2\pi)^3 \det(\hat{\Sigma}_t)}} \\ &\cdot \exp\left(-\frac{1}{2}(\hat{\mathbf{x}}_t - \mathbf{x}_t^*)^T \hat{\Sigma}_t^{-1} (\hat{\mathbf{x}}_t - \mathbf{x}_t^*)\right) \end{aligned} \quad (9)$$

and we apply negative log-likelihood to formulate the minimization as

$$\text{minimize } \frac{1}{2} \log((2\pi)^3 \det(\hat{\Sigma}_t)) + \frac{1}{2} (\hat{\mathbf{x}}_t - \mathbf{x}_t^*)^T \hat{\Sigma}_t^{-1} (\hat{\mathbf{x}}_t - \mathbf{x}_t^*) \quad (10)$$

where  $\det(\cdot)$  is the determinant of matrix. Based on the analysis, by discarding the constant terms, we can simply derive the third loss  $\mathcal{L}_3$  for end-to-end training of the sequential localization as

$$\mathcal{L}_3 = \frac{1}{k} \sum_{t-k}^t (\hat{\mathbf{x}}_t - \mathbf{x}_t^*)^T \hat{\Sigma}_t^{-1} (\hat{\mathbf{x}}_t - \mathbf{x}_t^*) + \beta \cdot \det(\hat{\Sigma}_t) \quad (11)$$

where  $\beta$  is a constant balance factor, and  $k$  denotes the length of sequence for training. This loss forms a balance between the likelihood and a lower uncertainty in the posterior.

### D. Implementation and Training Strategy

We implement the proposed system using Python and PyTorch. The whole network is trained on a single Nvidia Titan X GPU. As for the motion model in the KF, the ICP based radar odometry is implemented by using libpointmatcher [35].

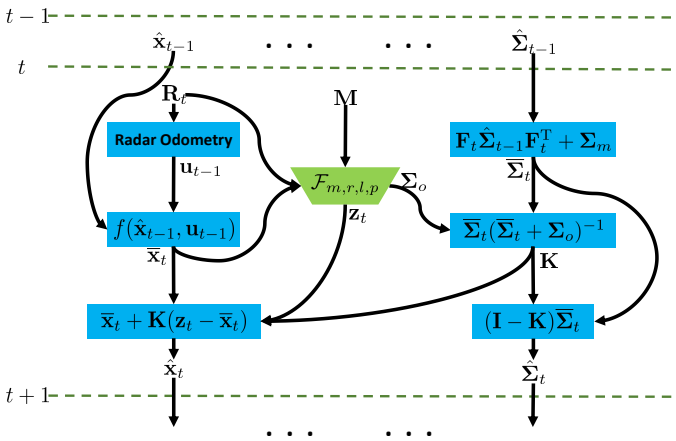


Fig. 4. The computation graph of Kalman filter for estimation at time  $t$ , in which the neural networks are integrated to provide measurements.

We first train the measurement model  $\mathcal{F}_{\mathcal{L}_1+\mathcal{L}_2}$  using the single step loss  $\mathcal{L}_1 + \mathcal{L}_2$ . The training and test data is augmented by randomly sampling the initial poses near the ground truth poses. The sensitivity analysis and comparisons are conducted in Section IV-B and IV-D by using  $\mathcal{F}_{\mathcal{L}_1+\mathcal{L}_2}$ . Furthermore, the pre-trained network is then trained with the sequential loss  $\mathcal{L}_3$  in an end-to-end manner, denoted as  $\mathcal{F}_{\mathcal{L}_1+\mathcal{L}_2,\mathcal{L}_3}$ . The input data for training  $\mathcal{F}_{\mathcal{L}_1+\mathcal{L}_2,\mathcal{L}_3}$  is sequences of temporal radar scans and corresponding ground truth poses. The pose tracking tests with the trained  $\mathcal{F}_{\mathcal{L}_1+\mathcal{L}_2}$  and  $\mathcal{F}_{\mathcal{L}_1+\mathcal{L}_2,\mathcal{L}_3}$  are presented in Section IV-C.

#### IV. EXPERIMENTS

In Section IV-A, we first introduce the datasets for evaluation, then followed an ablation study in Section IV-B. The performance of pose tracking and localization are presented in Section IV-C and IV-D, with comparisons to recent methods.

##### A. Datasets

We conduct the experiments on the public autonomous driving datasets, Oxford Radar RobotCar (RobotCar)<sup>2</sup> [15], [16] in UK and Multimodal Range Dataset (MulRan)<sup>3</sup> [17] in South Korea. Both of these datasets include ground truth poses, extrinsic calibration, raw lidar and radar data. The sensors types and locations on vehicles are different in the two datasets, thus validating the generalization of the proposed method indirectly.

Table I and Table II present the details of the sequences in these two datasets. For RobotCar dataset, we select six sequences at different time, and Oxford-01 is used for mapping and network training. To validate RaLL in this paper, we follow the path split in [27], shown in Figure 6(a). As for MulRan dataset, sessions at DCC, KAIST and Riverside are used for evaluation. We build the laser maps using DCC-01, KAIST-02 and Riverside-02, and generalize all sequences directly using the learned model in RobotCar. This generalization strategy is performed in all the following experimental sections IV-B, IV-C and IV-D.

<sup>2</sup><https://oxford-robotics-institute.github.io/radar-robotcar-dataset>

<sup>3</sup><https://sites.google.com/view/mulran-pr>

TABLE I  
SEQUENCES 01-06 OF ROBOTCAR DATASET AT OXFORD

Date	Len.(km)	Sequence
10/01/2019	9.02	Oxford-01: mapping & training
10/01/2019	9.04	Oxford-02: localization test
11/01/2019	9.03	Oxford-03: localization test
16/01/2019	9.01	Oxford-04: localization test
17/01/2019	9.02	Oxford-05: localization test
18/01/2019	9.01	Oxford-06: localization test

TABLE II  
SEQUENCES OF MULRAN DATASET AT KAIST, DCC AND RIVERSIDE

Date	Len.(km)	Sequence (Generalization)
02/08/2019	4.91	DCC-01: mapping & test
23/08/2019	4.27	DCC-02: localization test
03/09/2019	5.42	DCC-03: localization test
20/06/2019	6.13	KAIST-01: localization test
23/08/2019	5.97	KAIST-02: mapping & test
02/09/2019	6.25	KAIST-03: localization test
02/08/2019	7.25	Riverside-01: localization test
16/08/2019	6.61	Riverside-02: mapping & test

##### B. Ablation Study on Various Configurations

First of all, we employ the sensitivity analysis on the input range images, including the scan size  $H, W$  and resolution  $r$ . Input radar scans and lidar maps share four types of image settings, as shown in Figure 5(a); and then four networks are trained with these different inputs. The parameter  $k$  varies when  $H = W = 256$  or  $512$  relatively, thus guaranteeing the invariance of input patch sizes for patch networks. The ablation study is manual labor consuming for training networks, but we consider it is worthy to explore an appropriate solution for radar localization.

We set the offset in the limit range as follows:  $\Delta x_m = \Delta y_m = 2m$ , and  $\Delta \theta_m = 2^\circ$ , and also set the resolution  $\delta x = \delta y = 2m, \delta \theta = 2^\circ$  in solution space, thus the cost volume is divided to  $n_{xy\theta} = 3 \times 3 \times 3$ . Samples are generated randomly with known offsets for training and evaluation. In RobotCar dataset, we collect more than 1000 samples in the test path of Oxford-02 and Oxford-03; and more than 3000 samples in DCC-02 and KAIST-02 of MulRan dataset. The estimated offset is inferred by the trained networks  $\mathcal{F}_{\mathcal{L}_1+\mathcal{L}_2}$ . We calculate the mean errors of the estimated offsets alongside the three dimensions  $x, y, \theta$  in robot coordinate.

The evaluation results are shown in Figure 5(a). It is obvious that the neural networks performs best than the others when  $H = W = 512$  and  $r = 0.25m/pixel$ . And the network also works well with  $H = W = 256$  and  $r = 0.5m/pixel$ . In summary, conclusions can be drawn from these comparisons: the higher range resolution is, or the longer detection range is, the more precise estimation will be achieved. But due to the constrained resources, it is a tradeoff between the image sizes and computing efficiency.

Based on the ablation analysis above, the best two con-

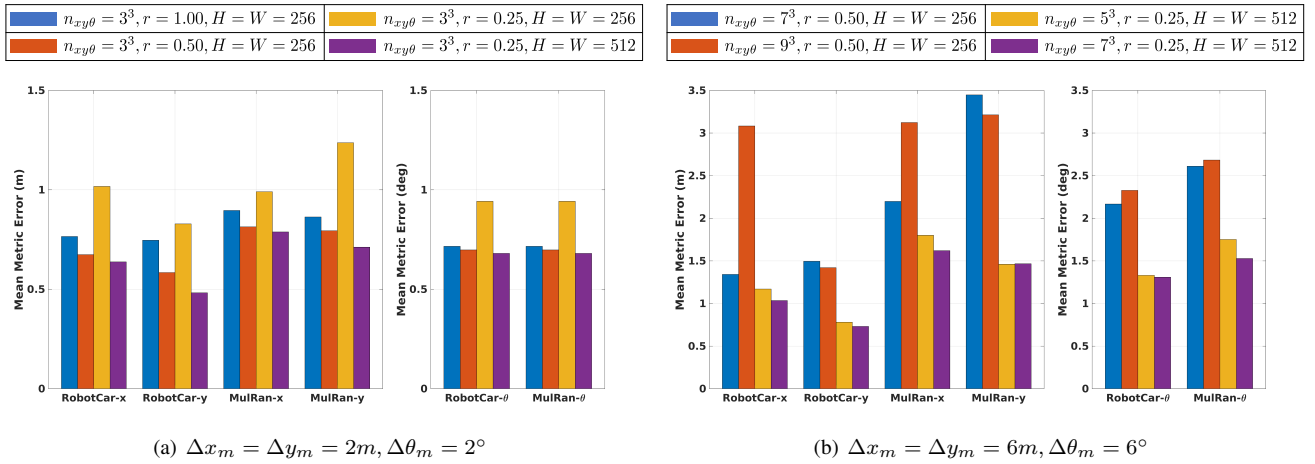


Fig. 5. We conduct the sensitivity experiments with various configurations, and conclusions can be drawn after comparisons and analysis.

TABLE III  
RMSE OF ABSOLUTE TRAJECTORIES

Dataset	Sequence	Fake-Lidar [28]		Radar Odometry		RaLL ( $\mathcal{F}_{\mathcal{L}_1+\mathcal{L}_2}$ )		RaLL ( $\mathcal{F}_{\mathcal{L}_1+\mathcal{L}_2,\mathcal{L}_3}$ )	
		Trans.(m)	Rot.( $^\circ$ )	Trans.(m)	Rot.( $^\circ$ )	Trans.(m)	Rot.( $^\circ$ )	Trans.(m)	Rot.( $^\circ$ )
RobotCar	Oxford-02	8.46	5.43	263.27	26.93	1.42	1.53	<b>0.98</b>	<b>1.45</b>
	Oxford-03	6.93	2.46	229.95	17.04	1.65	1.66	<b>1.14</b>	<b>1.62</b>
	Oxford-04	9.12	4.47	131.66	11.16	2.18	2.00	<b>1.71</b>	<b>1.93</b>
	Oxford-05	-	-	439.23	44.14	1.47	1.57	<b>1.11</b>	<b>1.48</b>
	Oxford-06	14.10	4.25	333.04	19.45	1.52	1.57	<b>1.14</b>	<b>1.52</b>
	MulRan	DCC-01	-	-	218.47	51.41	2.90	2.01	<b>2.11</b>
DCC-02		-	-	96.96	21.90	5.10	2.28	<b>4.71</b>	<b>2.01</b>
DCC-03		-	-	146.28	33.64	5.88	2.75	<b>5.14</b>	<b>2.55</b>
KAIST-01		-	-	376.97	65.04	1.98	1.88	<b>1.45</b>	<b>1.74</b>
KAIST-02		-	-	216.47	47.43	1.86	1.79	<b>1.30</b>	<b>1.71</b>
KAIST-03		-	-	242.72	39.56	1.97	1.60	<b>1.27</b>	<b>1.50</b>
Riverside-01		-	-	367.30	39.61	497.82	48.09	<b>4.12</b>	<b>2.84</b>
Riverside-02		-	-	407.65	32.04	9.52	3.19	<b>2.52</b>	<b>1.93</b>

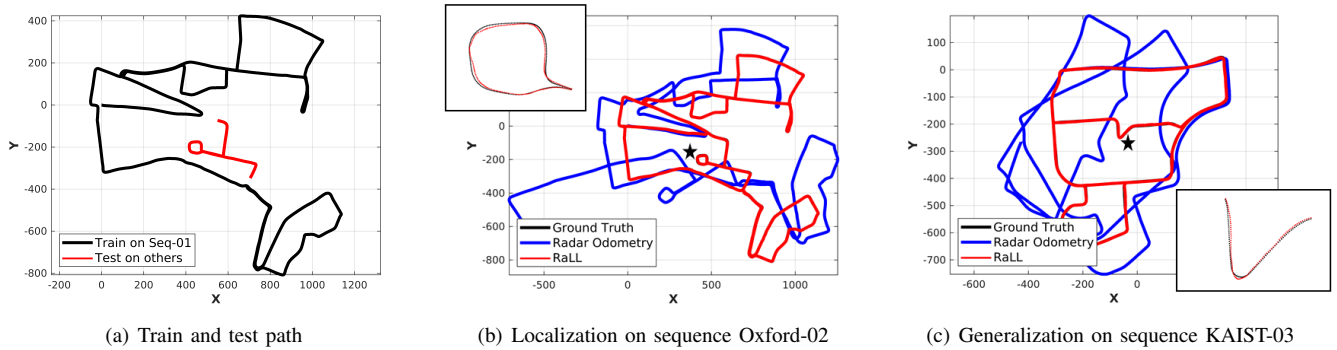


Fig. 6. (a) We split the data in RobotCar dataset for training and evaluation, and the overlapping area is removed. (b) The pose tracking on Oxford-02, including a zoomed view at \* location. (c) The learned model is also generalized to new environments in MulRan dataset.

figurations are selected to further experiments. We extend the offset to  $\Delta x_m = \Delta y_m = 6m$ , and  $\Delta \theta_m = 6^\circ$ . In this solution space, different resolutions  $\delta x, \delta y, \delta \theta$  are tested, resulting various  $n_{xy\theta}$  shown in Figure 5(b). From the evaluation results, it is obvious that the neural networks achieve

best performance with  $n_{xy\theta} = 7^3$  and  $r = 0.25m/pixel$ . The comparison between  $9^3$  and  $7^3$  when  $r = 0.5m/pixel$  shows that higher resolution in offset space may not bring more precise estimation. We think it is because of the limited neurons in the network, which is hard to learn the distribution

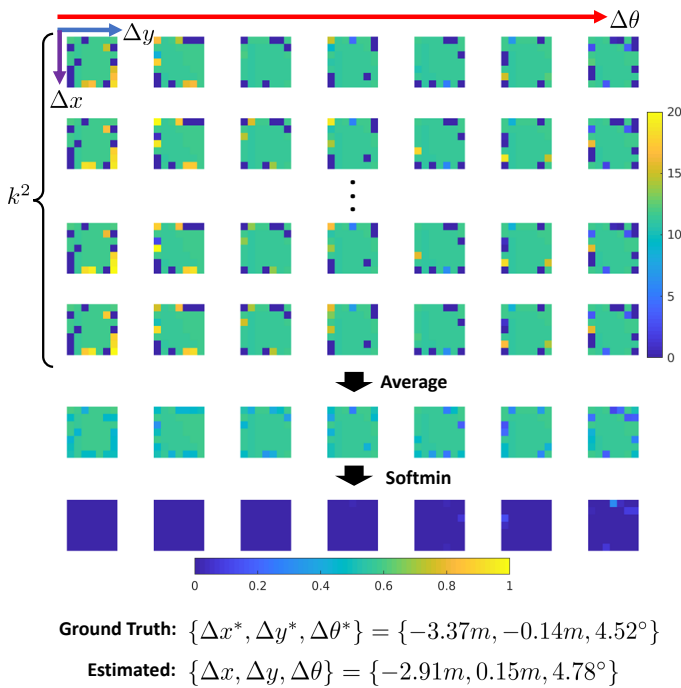


Fig. 7. The visualization of the output results from networks. The tensors and probabilities are expanded along the  $\{\Delta x, \Delta y, \Delta \theta\}$  axes.

TABLE IV  
ABSOLUTE TRAJECTORY ERROR IN COMPARISON WITH PHARAO

Dataset	Translation Error (m)		
	PhaRaO [12] (Registration)	PhaRaO [12] (Full Module)	RaLL
DCC-02	132.78	12.08	<b>4.71</b>
Riverside-02	83.93	31.83	<b>2.52</b>

of a large number of possibilities.

From these extensive ablation experiments, we also notice that the error in  $x$  is often larger than  $y$ , which are longitudinal and lateral axes for automotive vehicles relatively. We consider this result is interpretable due to the road environments in the two autonomous driving datasets. Most of the roads are straight for vehicles, and are more distinguishable along the lateral direction, especially when there are few features on the road sides. Therefore, it is more difficult to estimate the  $\Delta x$  than  $\Delta y$  in this paper.

### C. Pose Tracking Evaluation

For the experiments in Section IV-C and IV-D, we select the best configuration in IV-B:  $H = W = 512$ ,  $r = 0.25m/pixel$ , and the volume is set as  $n_{xy\theta} = 7^3$  for estimation in  $\Delta x_m = \Delta y_m = 6m$ ,  $\Delta \theta_m = 6^\circ$ .

The pose tracking is performed on the whole path of the test sequences. To compare the performance, we accumulate the proposed radar odometry as a comparison, and this odometric localization results in large errors. The direct radar odometry PhaRaO in [12] was performed on DCC-02 and Riverside-02, and we also compare our method on these two sequences.

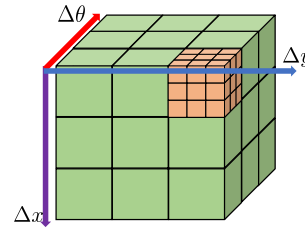


Fig. 8. Division of the solution space. Each green sub-space is divided again to obtain the  $\Delta \hat{x}_s$  inside.

TABLE V  
COMPARISONS OF LOCALIZATION WITH LARGE OFFSETS

Dataset	Method	Mean Metric Error		
		$x$ (m)	$y$ (m)	$\theta$ ( $^\circ$ )
RobotCar	RSL-Net [26]	3.41	2.66	2.45
	PASED [27]	<b>2.57</b>	2.21	2.65
	RaLL	3.51	<b>2.05</b>	<b>1.60</b>
MulRan	RSL-Net [26]	2.61	3.31	<b>1.40</b>
	PASED [27]	3.26	3.57	2.15
	RaLL (Gen.)	<b>2.43</b>	<b>2.03</b>	1.90

Additionally, RaLL is also compared to the localization system in [28], denoted as Fake-Lidar method.

Table III and Table IV present the Root Mean Squared Errors (RMSE) on position  $x - y$  and the orientation  $\theta$ , which are calculated on absolute trajectories in global coordinate. Figure 6(b) and Figure 6(c) present pose tracking results. It is obvious that RaLL with  $\mathcal{F}_{\mathcal{L}_1+\mathcal{L}_2,\mathcal{L}_3}$  produces the best performance, and both positional and orientational errors are in limited range. Furthermore, the end-to-end trained  $\mathcal{F}_{\mathcal{L}_1+\mathcal{L}_2,\mathcal{L}_3}$  performs better than  $\mathcal{F}_{\mathcal{L}_1+\mathcal{L}_2}$ , especially in the challenging Riverside of MulRan, which indicates that the effectiveness of the proposed differentiable models and sequential learning. In addition, we generalize the learned model on MulRan dataset without re-training, validating the robustness and feasibility of the proposed system.

We also present the visualization of a case study, as shown in Figure 7. The resulting tensor size from patch network  $\mathcal{F}_p$  is  $(k^2 \times n_{xy\theta} \times 1 \times 1)$ , and we formulate it to  $\{\Delta x, \Delta y, \Delta \theta\}$  axes for better visualization. After averaging of  $k^2$  tensors and softmin operation, the differences are transformed to the offset probabilities in the range of  $[0, 1]$ . Finally, the estimated pose offset  $\Delta \hat{x}$  is close to the ground truth  $\Delta x^*$  for pose tracking, and the visualization results demonstrate that our proposed networks have good interpretability.

### D. Localization with the Large Offsets

Besides the pose tracking task, we also perform the localization with large initial offset by using the proposed networks directly. This experiment is compared to the methods in [26], [27]. For a fair comparison, we expand the solution space to

$\Delta x_m = \Delta y_m = 18m, \Delta \theta_m = 18^\circ$ , which is close to the experiments in [26], [27], and is also a very large offset on pixel levels in this paper. More than 200 and 500 samples are generated in the test path of Oxford-02 and KAIST-02.

However, our proposed network is designed for limited offsets originally, and not applicable to large offsets. To achieve this goal, we divide the entire space to several sub-spaces, illustrated in Figure. 8. And initial guesses are raised in the center of these sub-spaces as initial offsets  $\{\Delta \mathbf{x}\}$ . Then the proposed network is applied at each initial offset, and we can obtain the estimated  $\{\Delta \hat{\mathbf{x}}_s\}$  in sub-spaces. While in the entire space, all the potential solutions are  $\{\Delta \mathbf{x} \boxplus \Delta \hat{\mathbf{x}}_s\}$ , and the problem is then transformed to find the best solution in this answer set. In Section III-B, the coarse similarity is measured by subtraction directly, and here we calculate this measurement for selection. Specifically, for every pair of embeddings, the individual similarity or difference is formulated as  $\|\mathbf{E}_t^r - \mathbf{E}_{t,ijk}^l\|_2$ . Finally, we regard the offset with minimum difference as the estimated offset.

The evaluation results are presented in Table V, and we exchange  $x$  and  $y$  in [26], [27] because of the different representations in methodologies. Our proposed method performs better overall the performance, compared to another two deep learning based methods. This experiment indicates that our network not only handles long-term pose tracking, but also the localization with large offsets.

## V. CONCLUSION

An end-to-end method RaLL is proposed in this paper, which can localize a rotating radar sensor on a prior laser map. We demonstrate the effectiveness of the proposed differentiable localization system in multi-session multi-scene datasets. In the future, we consider that a learned network is desired to replace the traditional filter method in the back-end, and the whole system can be data-driven completely.

## REFERENCES

- [1] R. Mur-Artal, J. M. M. Montiel, and J. D. Tardos, "Orb-slam: a versatile and accurate monocular slam system," *IEEE transactions on robotics*, vol. 31, no. 5, pp. 1147–1163, 2015.
- [2] Y. Jiao, Y. Wang, X. Ding, B. Fu, S. Huang, and R. Xiong, "2-entity ransac for robust visual localization: Framework, methods and verifications," *IEEE Transactions on Industrial Electronics*, 2020.
- [3] X. Ding, Y. Wang, R. Xiong, D. Li, L. Tang, H. Yin, and L. Zhao, "Persistent stereo visual localization on cross-modal invariant map," *IEEE Transactions on Intelligent Transportation Systems*, 2019.
- [4] P. Krüsi, B. Bücheler, F. Pomerleau, U. Schwesinger, R. Siegwart, and P. Furgale, "Lighting-invariant adaptive route following using iterative closest point matching," *Journal of Field Robotics*, vol. 32, no. 4, pp. 534–564, 2015.
- [5] W. Lu, Y. Zhou, G. Wan, S. Hou, and S. Song, "L3-net: Towards learning based lidar localization for autonomous driving," in *Proceedings of the IEEE Conference on Computer Vision and Pattern Recognition*, pp. 6389–6398, 2019.
- [6] I. A. Barsan, S. Wang, A. Pokrovsky, and R. Urtasun, "Learning to localize using a lidar intensity map," in *Conference on Robot Learning (CoRL)*, pp. 605–616, 2018.
- [7] A. Carballo, J. Lambert, A. Monroy, D. Wong, P. Narksri, Y. Kitsukawa, E. Takeuchi, S. Kato, and K. Takeda, "Libre: The multiple 3d lidar dataset," in *2020 IEEE Intelligent Vehicles Symposium (IV)*. IEEE, 2020.
- [8] S. H. Cen and P. Newman, "Precise ego-motion estimation with millimeter-wave radar under diverse and challenging conditions," in *2018 IEEE International Conference on Robotics and Automation (ICRA)*, pp. 1–8. IEEE, 2018.
- [9] S. H. Cen and P. Newman, "Radar-only ego-motion estimation in difficult settings via graph matching," in *2019 International Conference on Robotics and Automation (ICRA)*, pp. 298–304. IEEE, 2019.
- [10] R. Aldera, D. De Martini, M. Gadd, and P. Newman, "Fast radar motion estimation with a learnt focus of attention using weak supervision," in *2019 International Conference on Robotics and Automation (ICRA)*, pp. 1190–1196. IEEE, 2019.
- [11] D. Barnes, R. Weston, and I. Posner, "Masking by moving: Learning distraction-free radar odometry from pose information," in *Conference on Robot Learning (CoRL)*, pp. 303–316, 2020.
- [12] Y. S. Park, Y.-S. Shin, and A. Kim, "Pharao: Direct radar odometry using phase correlation," in *IEEE International Conference on Robotics and Automation (ICRA)*, 2020.
- [13] Z. Hong, Y. Petillot, and S. Wang, "Radarslam: Radar based large-scale slam in all weathers," *arXiv preprint arXiv:2005.02198*, 2020.
- [14] W.-C. Ma, I. Tartavull, I. A. Barsan, S. Wang, M. Bai, G. Mattyus, N. Homayounfar, S. K. Lakshminanth, A. Pokrovsky, and R. Urtasun, "Exploiting sparse semantic hd maps for self-driving vehicle localization," pp. 5304–5311, 2019.
- [15] D. Barnes, M. Gadd, P. Murcutt, P. Newman, and I. Posner, "The oxford radar robotcar dataset: A radar extension to the oxford robotcar dataset," *arXiv preprint arXiv:1909.01300*, 2019.
- [16] W. Maddern, G. Pascoe, C. Linegar, and P. Newman, "1 year, 1000 km: The oxford robotcar dataset," *The International Journal of Robotics Research*, vol. 36, no. 1, pp. 3–15, 2017.
- [17] G. Kim, Y. S. Park, Y. Cho, J. Jeong, and A. Kim, "Mulran: Multi-modal range dataset for urban place recognition," in *IEEE International Conference on Robotics and Automation (ICRA)*, 2020.
- [18] Y. S. Park, J. Kim, and A. Kim, "Radar localization and mapping for indoor disaster environments via multi-modal registration to prior lidar map," in *2019 IEEE/RSJ International Conference on Intelligent Robots and Systems (IROS)*, pp. 1307–1314. IEEE, 2019.
- [19] C. X. Lu, S. Rosa, P. Zhao, B. Wang, C. Chen, J. A. Stankovic, N. Trigoni, and A. Markham, "See through smoke: robust indoor mapping with low-cost mmwave radar," in *MobiSys*, pp. 14–27, 2020.
- [20] D. Vivet, P. Checchin, and R. Chapuis, "Localization and mapping using only a rotating fmcw radar sensor," *Sensors*, vol. 13, no. 4, pp. 4527–4552, 2013.
- [21] F. Schuster, M. Wörner, C. G. Keller, M. Haueis, and C. Curio, "Robust localization based on radar signal clustering," in *2016 IEEE Intelligent Vehicles Symposium (IV)*, pp. 839–844. IEEE, 2016.
- [22] F. Schuster, C. G. Keller, M. Rapp, M. Haueis, and C. Curio, "Landmark based radar slam using graph optimization," in *2016 IEEE 19th International Conference on Intelligent Transportation Systems (ITSC)*, pp. 2559–2564. IEEE, 2016.
- [23] M. Rapp, M. Barjenbruch, M. Hahn, J. Dickmann, and K. Dietmayer, "Probabilistic ego-motion estimation using multiple automotive radar sensors," *Robotics and Autonomous Systems*, vol. 89, pp. 136–146, 2017.
- [24] M. Gadd, D. De Martini, and P. Newman, "Look around you: Sequence-based radar place recognition with learned rotational invariance," in *2020 IEEE/ION Position, Location and Navigation Symposium (PLANS)*, pp. 270–276. IEEE, 2020.
- [25] D. Barnes and I. Posner, "Under the radar: Learning to predict robust keypoints for odometry estimation and metric localisation in radar," in *IEEE International Conference on Robotics and Automation (ICRA)*, 2020.
- [26] T. Y. Tang, D. De Martini, D. Barnes, and P. Newman, "Rsl-net: Localising in satellite images from a radar on the ground," *IEEE Robotics and Automation Letters*, vol. 5, no. 2, pp. 1087–1094, 2020.
- [27] T. Y. Tang, D. De Martini, S. Wu, and P. Newman, "Self-supervised localisation between range sensors and overhead imagery," in *Robotics: Science and Systems (RSS)*, 2020.
- [28] H. Yin, Y. Wang, L. Tang, and R. Xiong, "Radar-on-lidar: metric radar localization on prior lidar maps," *arXiv preprint arXiv:2005.04644*, 2020.
- [29] R. Li, S. Wang, and D. Gu, "Deepslam: A robust monocular slam system with unsupervised deep learning," *IEEE Transactions on Industrial Electronics*, 2020.
- [30] C. Chen, B. Wang, C. X. Lu, N. Trigoni, and A. Markham, "A survey on deep learning for localization and mapping: Towards the age of spatial machine intelligence," *arXiv preprint arXiv:2006.12567*, 2020.



- [31] A. Kendall, M. Grimes, and R. Cipolla, "Posenet: A convolutional network for real-time 6-dof camera relocalization," in *Proceedings of the IEEE international conference on computer vision*, pp. 2938–2946, 2015.
- [32] D. DeTone, T. Malisiewicz, and A. Rabinovich, "Superpoint: Self-supervised interest point detection and description," in *Proceedings of the IEEE Conference on Computer Vision and Pattern Recognition Workshops*, pp. 224–236, 2018.
- [33] O. Ronneberger, P. Fischer, and T. Brox, "U-net: Convolutional networks for biomedical image segmentation," in *International Conference on Medical image computing and computer-assisted intervention*, pp. 234–241. Springer, 2015.
- [34] P. J. Besl and N. D. McKay, "Method for registration of 3-d shapes," in *Sensor fusion IV: control paradigms and data structures*, vol. 1611, pp. 586–606. International Society for Optics and Photonics, 1992.
- [35] F. Pomerleau, F. Colas, R. Siegwart, and S. Magnenat, "Comparing icp variants on real-world data sets," *Autonomous Robots*, vol. 34, no. 3, pp. 133–148, 2013.